Noncontact fluorescence diffuse optical tomography of heterogeneous media

L. Hervé,* A. Koenig, A. Da Silva, M. Berger, J. Boutet, J. M. Dinten, P. Peltié, and P. Rizo

CEA-LETI, MINATEC, Grenoble F-38054, France

*Corresponding author: lionel.herve@cea.fr

Received 20 July 2006; revised 8 March 2007; accepted 3 April 2007;
posted 6 April 2007 (Doc. ID 73239); published 3 July 2007

Fluorescence-enhanced diffuse optical tomography is expected to be useful to the collection of functional information from small animal models. This technique is currently limited by the extent of tissue heterogeneity and management of the shape of the animals. We propose an approach based on the reconstruction of object heterogeneity, which provides an original solution to the two problems. Three evaluation campaigns are described: the first two were performed on phantoms designed to test the reconstructions in highly heterogeneous media and noncontact geometries; the third was conducted on mice with lung tumors to test fluorescence yield reconstruction feasibility *in vivo*. © 2007 Optical Society of America

OCIS codes: 170.0170, 170.3010, 170.3660, 260.2510.

1. Introduction

Near-infrared fluorescence-enhanced diffuse optical tomography (fDOT) is a cost effective method for obtaining quantitative functional measurements, which are used by the pharmacological industry for experiments on small animals. It consists of injecting target-specific fluorescent molecular probes [1] and reconstructing their bio-distribution [2,3]. fDOT enables both three-dimensional (3D) localization of the targeted areas and quantization of the local concentration of the fluorochromes. If cancer-specific markers are used, fDOT can be used to quantify the cancer activity and evaluate treatment efficiency.

Two challenges have to be addressed to make this technique attractive for commercial applications. First, since experiments on small animals are characterized by the very wide range of the excitation signal detected that depends on the nature of the diverse biological tissues crossed [4], the system has to be corrected to take account of attenuation heterogeneities. Two strategies are currently implemented by different groups to correct this: the first strategy is to reconstruct the medium optical parameters and diffusion and absorption coefficients using the diffuse optical tomography (DOT) method [5]. However, as demonstrated by Arridge *et al*. [6], such a method requires the use of acquisition chains with temporal capabilities (for the laser signal and detection) [7–10] to acquire complete sets of data, and are thus limited in practice by the restricted number of channels. A second strategy, proposed by Ntziachristos *et al*. for an approximate correction of optical heterogeneity measurements is to use Born normalization [11–13] and process the data as if the medium were homogeneous. Using this technique, fDOT data can be acquired with CCD detectors on continuous wave (cw) optical benches [7,12,13] and a personal computer can be used for reconstruction processing, making the device cost effective.

The second challenge for the fDOT technique is the management of complex geometries. At present, the technique is usually limited to simple geometries to simplify the propagation model and detection description. On small animal model experiments, it leads to immersing the animal in an index matching fluid [11] that needs to be renewed between experiments for sanitary reasons, thus reducing throughput significantly. The current strategy to solve this problem is to measure the external shape of the medium, typically using a laser scanner system. Knowledge of the boundary position is integrated in the fDOT reconstruction forward model by using Green's theorem [7,14,15] or the finite element method

0003-6935/07/224896-11$15.00/0

(FEM). Although these forward models include the correct boundary conditions, the simulated turbid medium is usually assumed to be homogeneous; [7,14,15] and correction of the small animal's intrinsic heterogeneities relies on Born normalization.

We have developed a fluorescence diffuse optical tomography fDOT instrument in our laboratory to conduct cancer detection experiments on small animals. To keep the cost of the instrument low, the excitation laser is continuous and detection is performed by a CCD camera. This paper presents a tractable numerical approach to address attenuation heterogeneity and complex external shape issues simultaneously. We will begin by presenting the theoretical background of fDOT measurements (propagation of light in the medium through Green's functions, their numerical computation, and the fluorescence yield reconstruction). This theoretical part also presents the optical heterogeneity computation method and how it can be used to address complex geometries. In the second part, we present the optical tomographer developed in our laboratory and three experimental campaigns to evaluate our approach. The first campaign was run on a phantom designed to test reconstruction in highly heterogeneous media. The results show that fDOT reconstructions with optical heterogeneity represent a significant improvement on methods that do not take optical heterogeneity into account in the forward model. The second experiment was performed on a complex shaped phantom to validate the reconstruction for noncontact geometry objects. Finally, a campaign was run on a mouse to test the feasibility of *in vivo* fluorescence yield reconstruction. We present reconstructions using the normalized Born approximation or the optical heterogeneity correction and the results obtained on the mouse, with or without immersion.

2. Method

A. Diffuse Optical Imaging Forward Model

As shown in Fig. 1, fDOT experiments consist of injecting light at wavelength λ_{ex} into a diffuse medium. This generates a diffusive wave (excitation), which propagates inside the medium and excites the markers' fluorescence. These markers create a second diffusive wave at the fluorescence wavelength (emission) λ_{em} with an intensity proportional to incident wave and marker concentration. In transmission geometry, a laser source scans one side of the studied medium and the signals transmitted at wavelengths λ_{ex} and λ_{em} are recorded on the opposite side by a CCD camera.

In highly scattering media ($\mu_a \ll \mu_s'$) and for cw sources, the diffusive wave complies with the diffusion model [5]:

$$(\nabla D \nabla - \mu_a)\Phi(\mathbf{r}) = -S(\mathbf{r}), \tag{1}$$

where $D = 1/(3\mu_s')$ is the diffusion coefficient with μ_s' as the reduced scattering coefficient, μ_a is the absorption coefficient, $S(\mathbf{r})$ is the source term, and $\Phi(\mathbf{r})$ is the photon density at position $\mathbf{r}$. In our case, as the density wave is generated by a laser source, $S(\mathbf{r})$ is proportional to a Dirac δ function. Partial current boundary conditions [16] are used at the top and bottom borders:

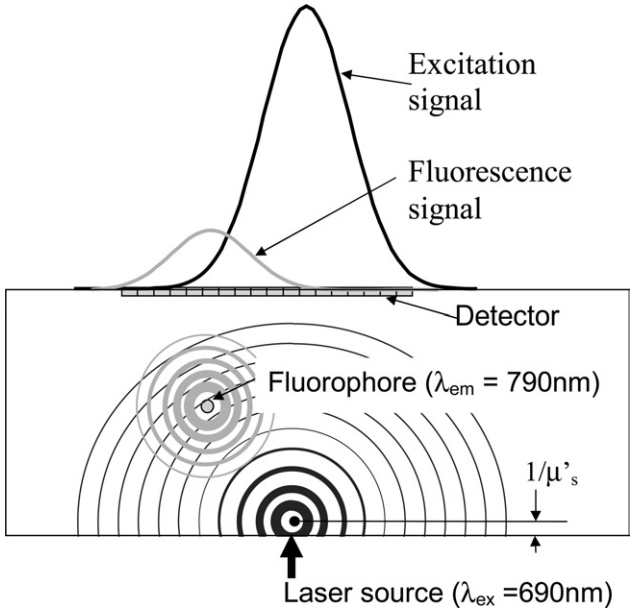

Fig. 1. Principal schema of fDOT measurements.

$$\frac{\partial \Phi(\mathbf{r})}{\partial \vec{n}} = -\alpha \Phi(\mathbf{r}), \tag{2}$$

where $\vec{n}$ is the normal vector to the boundary, and α is related to the index mismatch at the boundary. The light intensity transmitted through the medium for cw and monospectral experiments does not carry enough information to discriminate diffusion from absorption phenomena, as demonstrated by Arridge *et al*. [6]. Therefore, to prevent cross-talk when reconstructing these parameters, a more global parameter has to be considered. This is achieved by neglecting the variation of D [17], leading to a simpler form, a Helmoltz equation, for the propagation model:

$$(\nabla^2 - k^2)\Phi(\mathbf{r}) = -\hat{S}(\mathbf{r}), \tag{3}$$

where $k^2 = 3\mu_s'\mu_a$ expresses the "optical heterogeneity" and $\hat{S}(\mathbf{r}) = S(\mathbf{r})/D$ is the source term.

Our approach relies on the model expressed by Eq. (3) for describing light propagation. Even though various authors [18] have shown that Eq. (3) is not accurate for estimating optical parameters, we will demonstrate that, when the medium is optically heterogeneous, the fluorescence yield is better reconstructed when parameter k^2 is first estimated and we will also show how this parameter provides a way of working with noncontact measurements.

Given a k^2 map, we define Green's function $G(\mathbf{r_0}, \mathbf{r})$ which describes the propagation of light in a diffuse

medium from a source point $\mathbf{r_0}$ to a destination point $\mathbf{r}$ by

$$(\nabla^2 - k^2)G(\mathbf{r_0}, \mathbf{r}) = -\delta(\mathbf{r} - \mathbf{r_0}). \quad (4)$$

By using Eqs. (3) and (4) and since the sources (indexed by s) are modeled as Dirac delta functions (positioned at $1/\mu_s'$ inside the medium, see Fig. 1), the excitation density wave is given by

$$\Phi^{ex}(\mathbf{r_s}, \mathbf{r}) = \hat{\lambda} G(\mathbf{r_s}, \mathbf{r}), \quad (5)$$

where $\mathbf{r_s}$ is the position of the source s, $\mathbf{r}$ is a position inside the diffuse medium, and $\hat{\lambda}$ is a photometric factor related to laser power. Thus, $U^{ex}(\mathbf{r_s}, \mathbf{r_d})$ the excitation wave detected by the detector d at location $\mathbf{r_d}$ is

$$U^{ex}(\mathbf{r_s}, \mathbf{r_d}) = \lambda G(\mathbf{r_s}, \mathbf{r_d}), \quad (6)$$

where λ is a global factor taking into account laser power and detection efficiency which has to be calibrated on a reference homogeneous phantom in an auxiliary experiment.

If $X(\mathbf{r})$ is the fluorescence yield at position $\mathbf{r}$, by considering that light travels from positions $\mathbf{r_s}$ to $\mathbf{r}$ and from $\mathbf{r}$ to $\mathbf{r_d}$ and integrating on the whole volume Ω and, the fluorescence signal $U^{em}(\mathbf{r_s}, \mathbf{r_d})$ detected at detector d for laser excitation from source s, can be expressed as follows [19,20]:

$$U^{em}(\mathbf{r_s}, \mathbf{r_d}) = \lambda \int_{\Omega} G(\mathbf{r_s}, \mathbf{r}) X(\mathbf{r}) G(\mathbf{r}, \mathbf{r_d}) d\mathbf{r}. \quad (7)$$

Strictly speaking, $G(\mathbf{r_s}, \mathbf{r})$ describes light propagation at the excitation wavelength and $G(\mathbf{r}, \mathbf{r_d})$ corresponds to light propagation at emission wavelength. Therefore, these functions should be the solution to a set of *two* equations (4), one with the heterogeneity map at the excitation wavelength and the other at the emission wavelength. For the moment, to simplify computation and the experimental protocol, we assume that the G functions are similar at these two wavelengths.

B. Numeric Computations of the Forward Model

The system's Green's functions are obtained by the finite difference method. Therefore, we discretize the volume on a regular mesh (Fig. 2). Its typical voxel size is 1 mm for the z axis and 2 mm for the x and y axes. Even if the studied object does not present a parallelepipedic shape, a parallelepipedic mesh is chosen to include the studied object to allow for border effects.

Since solving Eq. (4) for a right hand side term equal to $\delta(\mathbf{r} - \mathbf{r_0})$ gives all the Green's functions $G(\mathbf{r_0}, \mathbf{r_m})$ for m describing all the indexes of the mesh, and since our method requires knowledge of $G(\mathbf{r_s}, \mathbf{r_m})$, $G(\mathbf{r_m}, \mathbf{r_d})$ and $G(\mathbf{r_s}, \mathbf{r_d})$ for s, d, and m describing all the indexes of the sources, detectors, and mesh points respectively, we can solve a set of equations (4) corresponding to the laser source and the detector positions. As the sources and detectors are not necessarily on the mesh grid, $G(\mathbf{r_0}, \mathbf{r_m})$ is evaluated for the neighboring nodes and the desired values are computed by linear interpolation. To compute $G(\mathbf{r_m}, \mathbf{r_d})$, we also use the mathematical property $G(\mathbf{r_m}, \mathbf{r_d}) = G(\mathbf{r_d}, \mathbf{r_m})$.

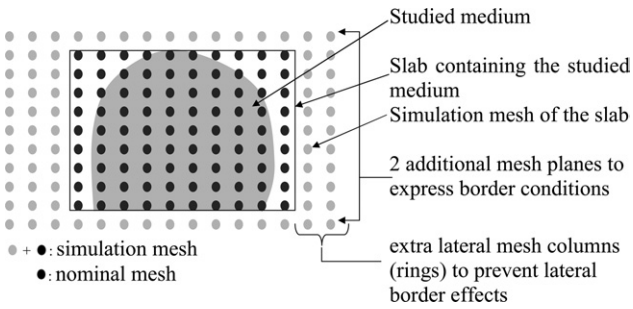

Fig. 2. Geometry of the simulation and the nominal meshes.

The Laplacian operator is replaced by its discretized version resulting in a sparse square matrix operator $(\nabla^2 - k^2)$ of dimension $M \times M$, where M is the number of mesh elements. To express the boundary conditions (2), two extra mesh planes are added; one at the top and one at the bottom of the simulation mesh (see Fig. 2). As lateral boundary conditions are given by $G(\mathbf{r_0}, \mathbf{r_m}) = 0$ for all $\mathbf{r_m}$ on the lateral borders, extra lateral columns are added (we chose to add four rings) to prevent the 0 constraint from interfering with the Green's function values in the region of interest.

From a typical nominal mesh of 2535 ($13 \times 13 \times 15$) elements for the object, after adding the two extra planes and four extra rings, we end up with a simulation mesh of 7497 ($21 \times 21 \times 17$) elements. For 100 sources and 400 detectors, the total procedure to determine $G(\mathbf{r_s}, \mathbf{r_m})$, $G(\mathbf{r_m}, \mathbf{r_d})$, and $G(\mathbf{r_s}, \mathbf{r_d})$ takes approximately 9 s with Matlab7 software running on a 3.2 GHz Intel Xeon processor. The Green's function values corresponding to the nominal mesh are stored in three matrices: G_{sm}, G_{md}, and G_{sd}. In this paper, we use G_{sm} to refer to the matrix as well as its elements $G_{sm}[s, m]$ to simplify notation and the same for G_{md} and G_{sd}.

C. Fluorescence Yield Reconstructions

When the G functions of the system are computed, we perform the fluorescence yield reconstruction by solving Eq. (8), which is obtained by discretizing Eq. (7) on the reconstruction (nominal) mesh:

$$U_{sd}^{em} = \lambda \Delta V \sum_m W_{sd}^{m} X_m, \quad (8)$$

where $U_{sd}^{em} = U_{sd}^{em}(\mathbf{r_s}, \mathbf{r_d})$, $X_m = X(\mathbf{r_m})$, ΔV is the unit volume and W_{sd}^{m} is a matrix with (number of sources) $\times$ (number of detectors) rows and M columns. Its matrix element is $W_{sd}^{m} = G_{sm} \times G_{md}$.

Fluorescence yield reconstruction consists of inverting Eq. (8) to find X_m. On simulated noisy data

acquisitions (SNR = 100) performed on a homogeneous medium containing a single fluorophore point, we determined that 16 algebraic reconstruction technique (ART) iterations, with a relaxation parameter set to 0.1, are sufficient to obtain a fit between projections and acquisitions better than the noise (decimation criterion). These parameters are kept for reconstruction in all cases.

Other authors [7,12,13] prefer to use a normalized approach, the normalized Born approximation, which consists of dividing Eq. (8) by Eq. (6):

$$\frac{U_{sd}^{em}}{U_{sd}^{ex}} = \frac{\sum_m G_{sm} X_m G_{md}}{G_{sd}} \Delta V. \tag{9}$$

Since the ratio U_{sd}^{em}/U_{sd}^{ex} corrects most of the system's heterogeneities [12,13] in a first approximation, the homogeneous G functions can be used. As we are seeking to reconstruct the fluorescence even in highly attenuating regions of small animals (typically mouse lungs, in which k^2 can reach 150 [4], to provide tools for lung tumor research), we found that this approximation was not sufficient. Later, we will present an efficient method to reconstruct optical heterogeneity of the probed medium.

D. Heterogeneity Reconstruction

To build G functions compatible with the heterogeneous medium, k^2 is reconstructed from the excitation signal. Let us consider the Rytov [21] expansion applied between a current system characterized by a heterogeneity map k^2 and the real system K^2:

$$\log\left(\frac{U^{ex}(\mathbf{r_s}, \mathbf{r_d})}{\lambda G(\mathbf{r_s}, \mathbf{r_d})}\right) \approx -\int_\Omega \frac{G(\mathbf{r_s}, \mathbf{r}) \Delta k^2(\mathbf{r}) G(\mathbf{r}, \mathbf{r_d})}{G(\mathbf{r_s}, \mathbf{r_d})} \, d\mathbf{r}, \tag{10}$$

where $\Delta k^2(\mathbf{r}) = K^2(\mathbf{r}) - k(\mathbf{r})^2$. The discretization of Eq. (10) leads to the following equation:

$$\forall (s, d), \qquad \log\left(\frac{U_{sd}^{ex}}{\lambda G_{sd}}\right) \approx -\sum_m \frac{G_{sm} \Delta k_m^{\,2} G_{md}}{G_{sd}} \Delta V, \tag{11}$$

where $\Delta k_m^{\,2} = \Delta k^2(\mathbf{r_m})$, $U_{sd}^{ex} = U^{ex}(\mathbf{r_s}, \mathbf{r_d})$ and ΔV is the unit volume. Given a set of G functions, Eq. (11) is a linear system for the unknown $\Delta k_m^{\,2}$. The equation is solved using a randomized ART algorithm with a positive constraint on $k_m^{\,2}$. However, as the G functions depend on the k^2 map, an iterative approach is required to solve the equation: first, we take a homogeneous k^2 map corresponding to reasonable physical values of the studied object, compute the corresponding G values from Eq. (4) using the current k^2 map and check if the convergence criterion, $\|U_{sd}^{ex} - \lambda G_{sd}\|$, where λ is the photometric factor defined in Eq. (6), is stabilized. If it is not, we reconstruct $\Delta k_m^{\,2}$ from Eq. (11) by ART, update $k_m^{\,2} \leftarrow k_m^{\,2} + \Delta k_m^{\,2}$ and return to the computation of the G functions. Empirically, for an ART relaxation parameter set to 0.01, eight iterations suffice to reach convergence. These parameters will be used for all the experimental acquisition processing presented hereafter.

E. Noncontact Handling

Most of the fDOT experiments are performed with fiber detectors in contact with the diffuse probed medium. Here, because we are using a CCD detector, as soon as the studied object ceases to be flat, the detector image cannot be entirely in contact with the surface of the phantom. Thus, the free-space propagation of the light from the studied diffuse medium to the detector must be considered.

Figure 3 shows a sketch of the free-space propagation of the light outside the diffuse medium. The detector element d is focused on the focal plane of the detector, which is not in contact with the object. However, as the diffusive phenomena create low frequency images and as we are working on undersampled images (20×20 pixel images), the field depth is large enough to consider that the detector remains focused. This detector element will be sensible to the specific intensity exiting the medium at $\mathbf{r_d}$ (see Fig. 3), the projection of the detector element onto the boundary of the studied medium following the direction of the mean optical ray. As the outgoing light is considered Lambertian, the specific intensity does not depend on the angle θ between the normal to the surface and the mean optical ray. Therefore, even if a CCD detector d is focused at the top of the object (position $\mathbf{R_d}$), we do as if it matches the boundary of the diffuse medium at $\mathbf{r}_d$. When the boundary is out of the detector's field depth, a more careful photometric derivation can be adopted [14].

One problem still remains with the approach presented here: a regular mesh including more than the studied object is used, therefore the boundary conditions defined in Eq. (2) are not applied in the right place (but at the top and the bottom of the mesh) resulting in erroneous G functions around the borders (and obviously outside the object). Equation (2) takes account of the fact that the light going outside the diffuse medium does not come back, leading the photon density wave to decrease around the boundaries. That can be similarly accounted for by additional attenuations in the surrounding medium. Therefore, a suitable $k^2(r)$ map, compounding intrin-

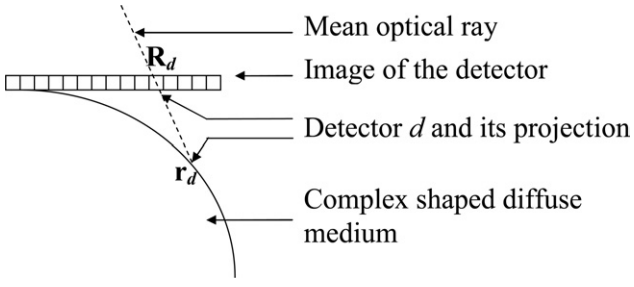

Fig. 3. Schema of the free-space propagation of the light outside the medium.

sic tissue heterogeneity and border effects, can describe the light propagation in the medium. By reconstructing this map from the excitation data, both effects are taken into account.

There are several advantages in the method presented here. It only requires knowledge of the medium boundaries at the detection point locations rather than the complete boundary. It does not need an implementation of the finite element method, thus leading to fast computation. Another expected advantage of the method is its robustness, since the boundary effect correction is consistent with CCD data acquisitions.

3. Approach Validation

A. Description of the Tomographer

The experiments presented in this paper were performed with the cw tomographer described previously (Fig. 4) [22]. The optical system is composed of a solid state laser source (690 nm, 17 mW) for illumination and a CCD camera (Orca EG, Hamamatsu) for detection. The source is guided to the object by an optical fiber. The scanning fiber is moved by two traveling plates (Microcontrol) and monitored by a computer. The 12-bit CCD camera is focused at the top surface of the probed object (phantoms or small animals).

For each source position, the transmitted light is acquired twice at both excitation and emission wavelengths. We controlled that the camera noise conforms to the manufacturer specification. Its quantum efficiency is around 50%, its conversion factor is 4.7 electrons per gray level, its read noise was characterized to be around 2 gray levels and its dark current was controlled to be a fraction of a gray level even after an 10 s duration acquisition and is therefore neglected. Since the whole camera dynamic is used, noise is limited by the photon statistics. Figure 5 summarizes the spectral characteristics of the acquisition chain. The emission signal is obtained using a filter (high pass RG9, Schott). To optimize transmission through the whole animal even in the liver or lung area, we chose to use a high wavelength fluorophore, Alexa 750 (Molecular Probes), whose emission peak is around 780 nm. To ensure that no excitation signal is detected as fluorescence, we decided to use a laser with a wavelength (690 nm) much lower than the fluorophore peak emission (780 nm), despite the low fluorophore absorption efficiency at this wavelength. An additional excitation band filter is used after the solid state laser to prevent any of its high energy light to be detected as an emission signal.

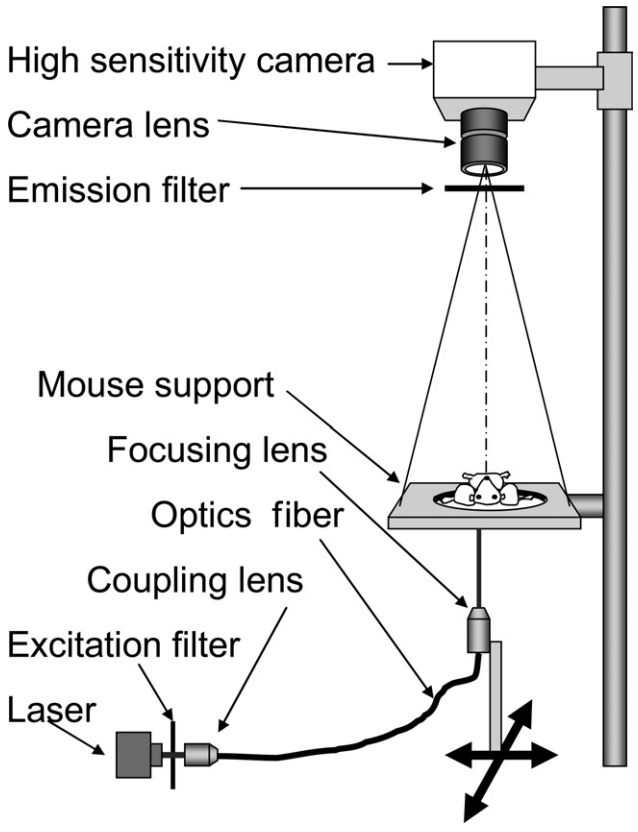

Fig. 4. Schema of the fDOT bench.

The excitation sources typically describe a regular 10×10 grid with 2 mm spacing and the CCD images regions of interest (typically 3 cm $\times$ 3 cm) are undersampled to form 20×20 pixel images. Thus, in this example, we have 400 measurements per source position, leading to 40,000 available measurements from the excitation acquisitions and 40,000 from the emission acquisitions. To accelerate reconstruction and improve its robustness, the less relevant measurement data were eliminated. For the optical heterogeneity map reconstruction, half (20,000) of the excitation measurements, corresponding to the couple source detector with the largest distance, were discarded from the data set. For the fluorescence reconstruction, half of the emission measurements, corresponding to the lower G_{sd}, were also discarded.

Overall system resolution, i.e., acquisition and reconstruction, was characterized by experiments in homogeneous liquid (intralipid) media containing two fluorescence (Alexa 750) point objects to be separated. Under these conditions, *x-y* resolution is roughly 1 mm, which is sharper than the reconstruction meshes used here. In the *z* direction, the system is able to distinguish between fluorescence dots set 4 mm apart, one above the other. The system was also characterized in an experiment with a single fluorescence dot embedded inside a 15 mm thick homogeneous medium (intralipid solution, $\mu_a = 0.2\ \mathrm{cm}^{-1}$, $\mu_s' = 10\ \mathrm{cm}^{-1}$). The results obtained (Fig. 6) for varying fluorophore concentrations (0.55, 1.1, 2.2, and 3.3 μmol/l) and *z* positions (6, 9, and 12 mm) show that the system is linear with respect to fluorescence concentration and independent of fluorescence inclusion depth.

The photobleaching of the Alexa750 fluorophore was characterized by repeating 12 complete scans on a homogeneous liquid phantom (intralipid solution, $\mu_a = 0.2\ \mathrm{cm}^{-1}$, $\mu_s' = 10\ \mathrm{cm}^{-1}$) containing a fluorescent tube at 3 mm from the source face. The signal was

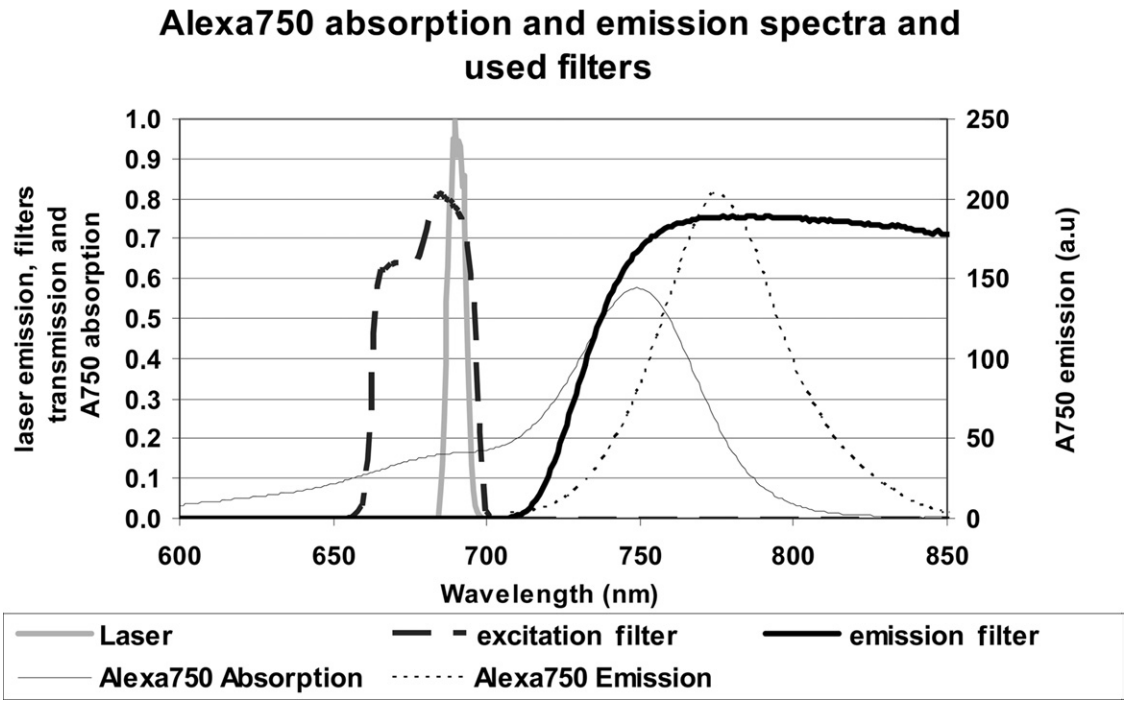

Fig. 5. Spectra measured on our system: laser, excitation filter, emission filter, and Alexa 750 absorption and fluorescence spectra.

found to decrease by 40% after this campaign, which corresponds to a 4% fluorescence decrease per scan. For the validations presented hereafter, since the fluorescent inclusions are positioned farther from the source face, the photobleaching will be much lower and will thus be neglected.

B. Results on a Heterogeneity Phantom

We designed a solid phantom that mimics small animal fluorescence tomography experiments to test our reconstruction method in the presence of highly heterogeneous media (Fig. 7). The phantom is composed of a mixture of epoxy resin (Solloplast), with titanium dioxide powder (Sigma-Aldrich) as the scatterer and black ink (Dalbe) as the absorber. The index of refraction is estimated to be 1.54, the reduced diffusion coefficient $\mu_s' = 10\ \mathrm{cm}^{-1}$, and the absorption coefficient $\mu_a = 0.2\ \mathrm{cm}^{-1}$. Three holes were drilled to insert fluorescent inclusions. These were thin glass tubes (external diameter: 3 mm, internal diameter: 2.4 mm, length: 3 cm) filled with fluorescent dyes (Alexa750, 10 μM, Molecular Probes), inserted in the phantom at a depth of 3.5 mm from the upper surface. To interfere with fluorescence emission, a hole 8 mm in diameter was drilled under the fluorescence region. It was filled with a mixture of water, intralipid (concentration 1%), and ink to create a highly attenuating medium whose optical characteristics are estimated to be $\mu_s' = 10\ \mathrm{cm}^{-1}$, $\mu_a = 2.0\ \mathrm{cm}^{-1}$, or with a lower attenuation mixture (concentration 1%, $\mu_a = 0.2\ \mathrm{cm}^{-1}$) to match the bulk material and obtain a homogeneous phantom.

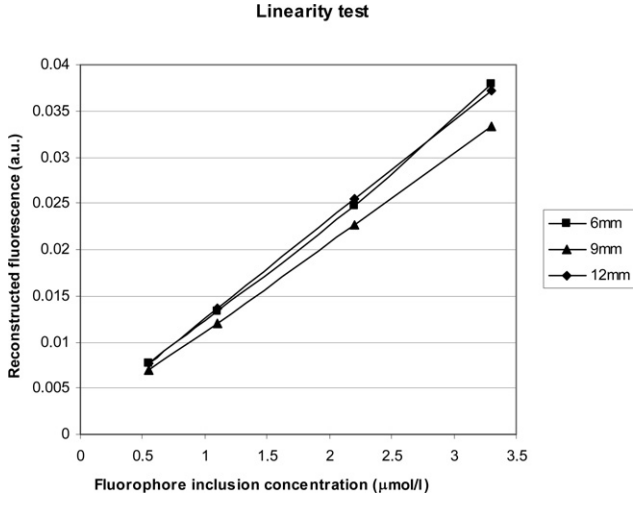

Fig. 6. Sum of the reconstructed fluorescence yield where the fluorophore dot is used inside a homogeneous 15 mm thick intralipid medium. Three z positions, i.e., 6, 9, and 12 mm, and four concentrations, i.e., 0.55, 1.1, 2.2, and 3.3 M (μmol/l) were tested.

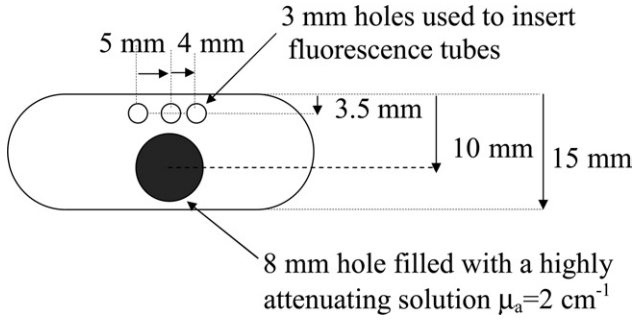

Fig. 7. Heterogeneous solid phantom used to validate reconstruction of the fluorescence yield in the presence of high attenuation.

In this experiment, 6×9 different equally spaced source positions, 2 mm apart, were considered. The acquisitions were then discretized on a regular 30×40 grid with points spaced by 0.5 mm. A reconstruction mesh composed of $13 \times 30 \times 18$ elements with a volume element of $0.2 \times 0.1 \times 0.1$ cm^3 was used. The sample rate was multiplied by two in the direction where spatial resolution can be lower (0.2 cm for x: parallel to the tube axes) to accelerate computation. The fluorescence yield reconstruction was achieved with ten ART iterations and a relaxation parameter of 0.1.

Reconstruction with no absorbers under the fluorescent inclusions showed a good separation of the three

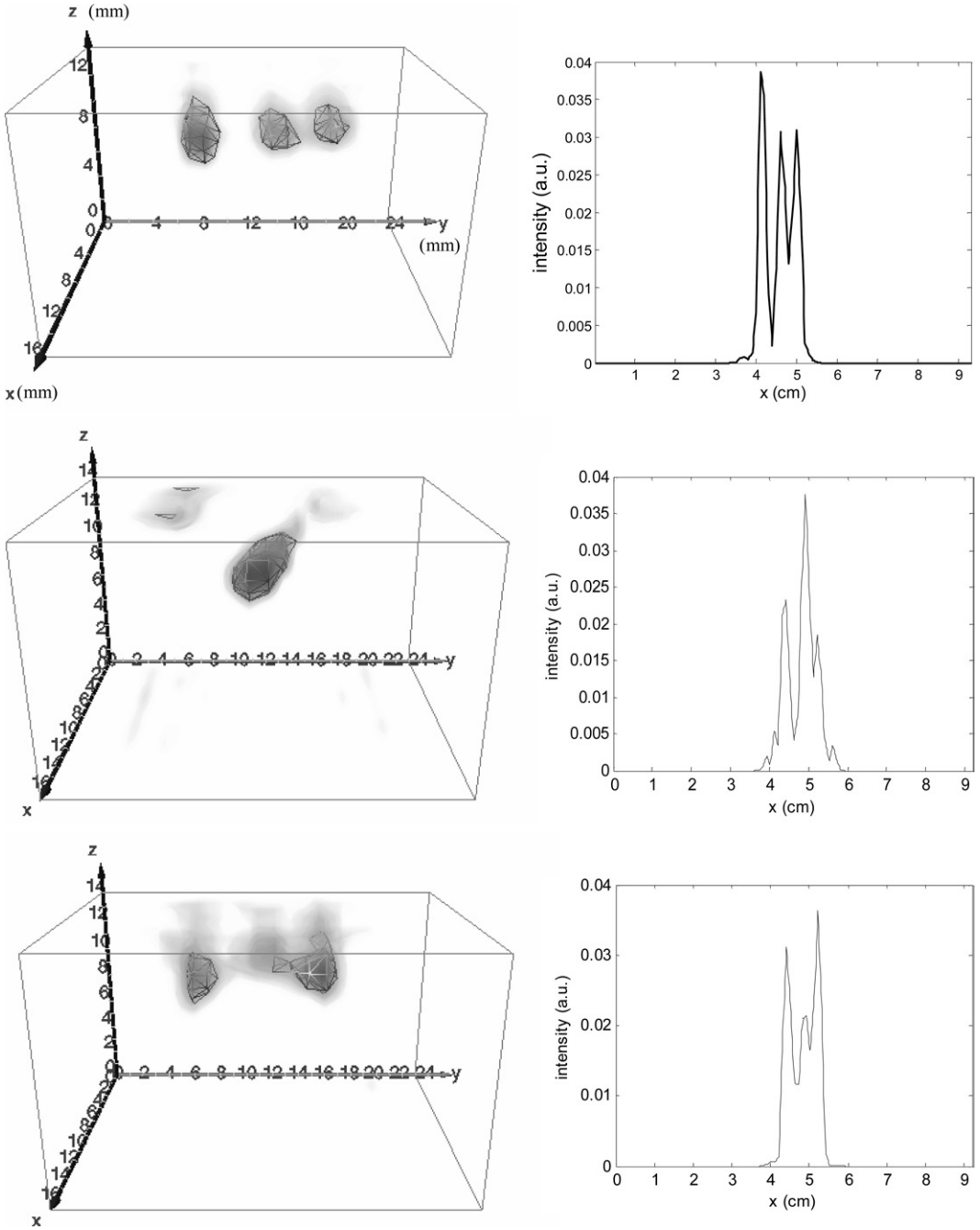

Fig. 8. 3D rendering (left) and y projection (right) of the reconstructed fluorescence yield of the heterogeneity phantom. (Top) Reconstruction of the heterogeneous solid phantom in the absence of high attenuation. The three fluorescence regions are well separated and positioned. (Middle) Reconstruction of the heterogeneous solid phantom in the presence of high attenuation using the Born ratio. The three fluorescence regions are not separated in the profile. The central fluorescence is overestimated and tends to merge with its nearest neighbor. The lateral fluorescence regions are underestimated and positioned too high. (Bottom) Reconstruction of the heterogeneous solid phantom in the presence of high attenuation using heterogeneity correction. The three fluorescence regions are separated and the positions of the three regions are correct, but the intensity of the central fluorophore is too low.

Table 1. Quantitative Results Obtained from the Fluorescence Yield Reconstruction of a Homogeneous Phantom When Using the Heterogeneity Correction Method[a]

	Fluorescence Sum (a.u.)	Mean of z (cm)	Standard Deviation on z (cm)
Tube 1 (left)	0.0082	1.17	0.24
Tube 2 (middle)	0.0073	1.18	0.21
Tube 3 (right)	0.0070	1.18	0.20

[a]Fluorescence yields, the recovered heights, and the widths of the reconstructed signal along z are stable from one tube to the other.

tubes, even for the two that were closest together, see Fig. 8 (top), showing the results as a 3D view of the reconstructed volume and a slice perpendicular to the tubes axes. Table 1 presents quantitative figures, i.e., the fluorescence yield amount ($=\sum_m X_m$), the mean of the z position ($\bar{z} = \sum_m X_m z_m / \sum_m X_m$) and the width along z expressed in term of standard deviation [$\sigma(z) = \sqrt{\sum_m X_m (z_m - \bar{z})^2 / \sum_m X_m}$], extracted from the fluorescence reconstruction of each tube. In the previous formulae, X_m is the fluorescence yield reconstructed at the mesh point m and z_m is the height of the mesh point m. We note that the recovered fluorescence is stable from one tube to the other (15% variation), that the positions of the three tubes are very accurate (the error is around 0.03 cm), and the widths along z of the three tubes are equivalent (around 0.2 cm).

The representations of the reconstruction in the presence of the absorber are shown in Fig. 8 (middle and bottom). The fluorescence yield reconstructed using the normalized Born ratio correction (11) is shown in Fig. 8 (middle) to enable comparison. With this method, the fluorescence tube just above the absorber was not reconstructed correctly since it was overestimated and tended to merge with its nearest neighbor. The lateral fluorescence regions were underestimated and positioned too high. From the quantitative figures presented in Table 2, we note that mean the height of the fluorescence yield reconstruction is correct (the discrepancy is around 0.05 cm). However, the reconstructed fluorescence amount of the central tube is exaggerated by 50% compared to the side tubes, and the widths of the

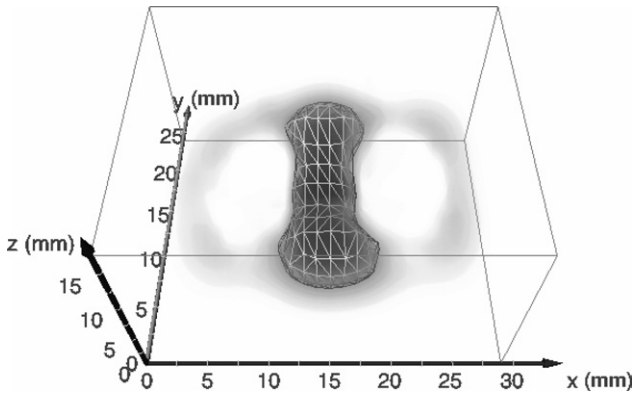

Fig. 9. Reconstructed map of heterogeneities. The absorber cylinder is correctly reconstructed.

three tubes are very different since the central tube is reconstructed four times flatter (0.09 cm) than the side tubes (0.43 cm) leading to the very heterogeneous concentration of the three tubes as presented in Fig. 8 (middle).

By taking into account the heterogeneity map (Fig. 8-bottom), most of the problems are solved. The reconstruction of the heterogeneity map shows the 8 mm cylinder filled with absorber (see Fig. 9). When this map is used during fluorescence yield reconstruction, the three separated tubes are distinguishable (Fig. 8-bottom), are correctly positioned and the intensities of the three fluorescence tubes are more similar. Table 3 presents the quantitative figures extracted from the reconstruction of the fluorescence yield of each tubes. We note that the reconstructed mean height is accurate (error below 0.06 cm), and, when compared to Table 2, the fluorescence sums are more similar (error around 20% between tube 3 and the two others) and the recovered widths of the three tubes are more stable (from 0.16 cm for the central tube to 0.21 cm for the side tubes).

C. Results in a Noncontact Geometry

A half cylinder solid phantom was designed to validate the noncontact approach developed above (Fig. 10). The bulk material of the phantom was the same composition as in the previous experiment. Two

Table 2. Quantitative Results Obtained from the Fluorescence Yield Reconstruction of the Heterogeneity Phantom When Using the Normalized Born Approximation[a]

	Fluorescence Sum (a.u.)	Mean of z (cm)	Standard Deviation on z (cm)
Tube 1 (left)	0.0091	1.15	0.39
Tube 2 (middle)	0.0138	1.10	0.09
Tube 3 (right)	0.0090	1.16	0.43

[a]Fluorescence yield varies by 50% from the central tube to the side tube and the recovered height is accurate (<0.5 mm, expected value = 1.15 cm). Widths along z of the fluorescence yield distribution are very different from the central tube to the side tube since their standard deviation varies by a factor of 4.

Table 3. Quantitative Results Obtained from the Fluorescence Yield Reconstruction of the Heterogeneity Phantom When Using the Heterogeneity Correction Method[a]

	Fluorescence Sum (a.u.)	Mean of z (cm)	Standard Deviation on z (cm)
Tube 1 (left)	0.0106	1.13	0.21
Tube 2 (middle)	0.0104	1.11	0.16
Tube 3 (right)	0.0125	1.09	0.21

[a]Fluorescence varies by 20% from tube 3 to tubes 1 and 2 and the recovered height is accurate (<0.6 mm, expected value = 1.15 cm). Widths along z of the fluorescence yield distribution are homogeneous between the three capillaries (0.21 cm for tubes 1 and 3, and 0.16 for tube 2).

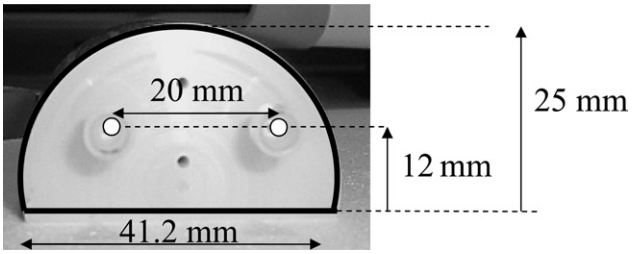

Fig. 10. Schema of the resin phantom (units of mm) with two tubes filled with Alexa750 fluorophores merged with its photograph.

holes, 20 mm apart, were drilled 12 mm from the ground surface for tube insertion.

In this experiment, 12×7 different, equally spaced source positions, 3 mm apart, were considered, corresponding to a rectangular field of view of approximately 3.3×1.8 cm^2. The CCD camera images of the phantom were resampled to create 20×20 pixel images covering a 3.6×2.5 cm^2 field of view. A nominal reconstruction mesh composed of $21 \times 16 \times 15$ elements with a volume element of $0.3 \times 0.3 \times 0.18$ cm^3 was used.

As described in the theoretical part, the method requires knowledge of the detector element projections on the phantom boundary. To compute these projections, the phantom shape must be described, in this case, by the geometrical specification of the phantom. Its (x, y) location was determined by using the picture taken with the acquisition camera. In the future, we intend to use a laser scanner to perform surface measurements.

Even though the phantom bulk material was homogeneous, we reconstructed the k^2 map to account for border conditions as explained above (eight ART iterations, relaxation parameter set to 0.01). Figure 11 shows a representation of this map. As suggested by the theoretical part, high attenuation was found close to the border of the phantom, since the light intensity is reduced in this area.

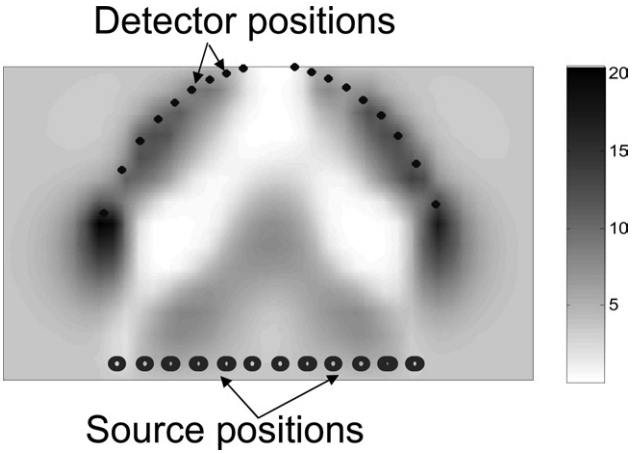

Fig. 11. Projection of the reconstruction of the k^2 map along the cylinder axis. We notice that the boundaries of the phantom are interpreted as high attenuation material (shown by the dark areas).

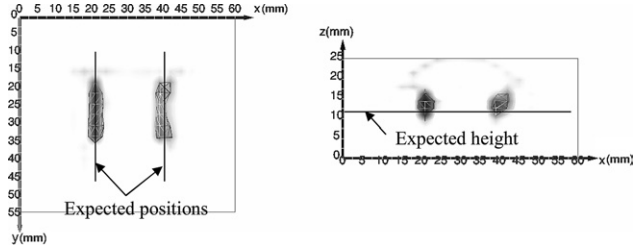

Fig. 12. Noncontact phantom reconstructions, xy and xz planes.

The fluorescence yield reconstruction was performed with ten ART iterations with a relaxation parameter set to 0.1. Two views of the volume reconstruction are shown in Fig. 12. This figure shows that the two fluorescence tubes are correctly reconstructed (shape) and are close to the expected position. Table 4 presents the quantitative figures obtained from the fluorescence reconstruction. We note that the recovered fluorescence amount is stable from tube 1 to tube 2 (10% variation), that the reconstructed position is correct (the recovered height 1.3 cm instead of 1.2 cm) and that the reconstructed widths along z of the tubes are equivalent.

D. *In Vivo* Results

To further validate the method presented, an fDOT experiment was conducted on a live nude mouse with a 14-day mammary murine lung tumor. The mouse was injected with 150 μg of Transferrin/Alexa 750 3 h before image acquisition. To test our noncontact management method, the mouse was imaged with and without the index matching liquid (intralipid). Using the immersion technique, it is possible to work with slab geometry [infinite in (x, y) directions]. During this acquisition, a thermal resistor was placed inside the liquid to maintain the animal's body temperature. The acquisitions were typically performed on regular 11×11 source positions with a 2 mm sampling rate in each direction. This corresponds to an acquisition time of around 20 mn. A reduced grid of 7×7 sources was used for reconstruction. The acquisitions were then discretized on a regular 33×33 grid with points spaced by 0.875 mm. A reconstruction mesh composed of $14 \times 14 \times 15$ elements with a volume element of $0.2 \times 0.2 \times 0.1$ cm^3 was used.

Table 4. Quantitative Results Obtained from the Fluorescence Yield Reconstruction of the Noncontact Phantom[a]

	Fluorescence Sum (a.u.)	Mean of z (cm)	Standard Deviation on z (cm)
Tube 1 (left)	0.0106	1.32	0.17
Tube 2 (right)	0.0097	1.34	0.18

[a]Fluorescence yield varies by 10% from tube 1 to tube 2, the recovered height is 0.1 cm higher than the expected value (1.2), and the widths along z of the fluorescence yield distribution are comparable from tube 1 to tube 2.

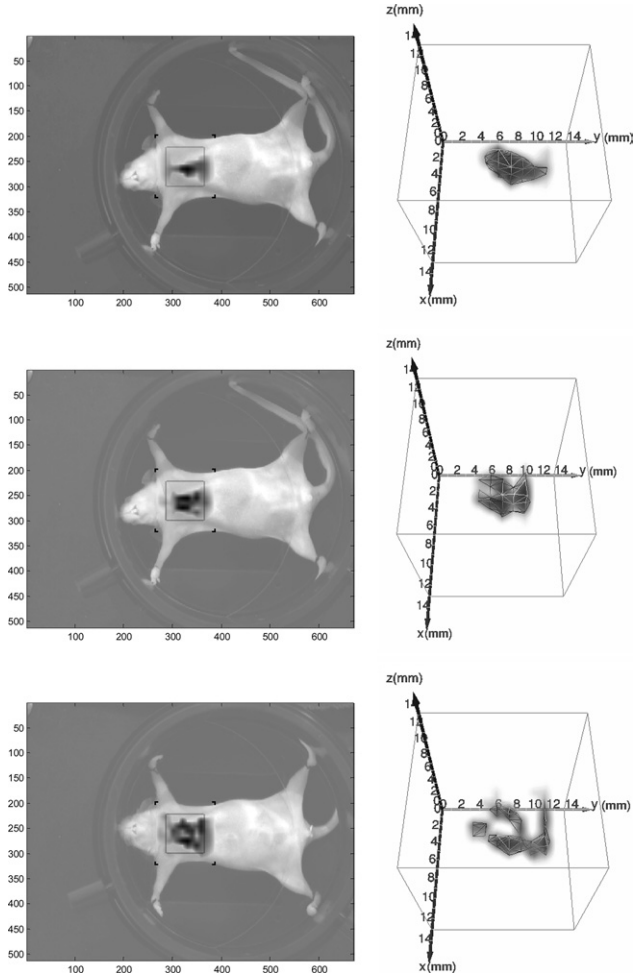

Fig. 13. Reconstruction results over the lungs, 3D representation of fluorochrome distribution reconstruction: (top) for a mouse immersed in adaptation liquid without taking into account heterogeneities, (middle) for a mouse immersed in adaptation liquid taking into account heterogeneities, (bottom) for a mouse without adaptation liquid taking into account heterogeneities. The gray scale is the same in the three cases.

Figure 13 presents the reconstructed volume in the lung area for this mouse. The upper images show the fluorescence yield reconstruction of the immersed mouse using the normalized Born approach (11). The fluorescence yield reconstructed in the lung area forms a homogeneous volume. The middle images were obtained taking into account the heterogeneities using the approach described above. Compared to the upper images, there are now two separate lobes in the lung area. A third lobe corresponds to the liver. These findings have been compared to fluorescence reflectance imaging (FRI) signals obtained on the organs after dissection of the mouse, and consistency between these two methods is high. The bottom reconstruction was obtained from the experiment without index matching liquid, where the mouse was positioned between two glass plates. As explained previously, the method presented here only requires knowledge of the position of the detection point. Therefore, this condition is met without measuring the mouse boundary by only considering the measurements in contact with the upper plate. The result can be compared to the result with index matching liquid which also shows three hot points, corresponding to the lungs and liver. The remaining differences between the two reconstructions may be due to the fact that fewer equations are used for the reconstruction process in the case of the mouse placed between the two glass plates.

Further studies will have to be carried out to take into account the mouse shape to add noncontact measurements to the equation system. More extensive results of fDOT *in vivo* measurements performed on the mouse with a lung tumor can be found elsewhere [23].

4. Discussion and Conclusion

The fDOT technique requires optical heterogeneity correction for small animal applications since the optical properties of the organs are significantly different [4]. To perform this correction on the light propagation model, another method (MRI, quantitative computed tomography, etc.) can be used to obtain quantitative information to be used *a priori* as in the fDOT technique. By using an all optical method, an exact approach would require temporal or frequential measurements to reconstruct the optical properties of the medium, with the distinction being made between diffusion and attenuation processes. However, the experimental setup is much more complex and expensive than a cw fDOT bench.

Here, we present a fDOT correction that consists of reconstructing a k^2 map from cw data. This map is an additional degree of freedom for the system to be consistent with the excitation measurements. It primarily represents the optical heterogeneity of the medium ($3\mu_a\mu_s'$), but in fact it also accounts for border effects (reduction of the photon density wave around the boundaries) and for various model description errors such as the detector positions. It significantly improves fluorescence yield reconstructions but its interpretation is not straightforward.

We designed two experiments to show the behavior of the k^2 reconstructed maps in the presence of heterogeneities and for noncontact geometries. In the first experiment, performed on a simple-shaped heterogeneous phantom, the reconstructed optical heterogeneity conformed well with the attenuation properties of the phantom. The subsequent fluorescence yield reconstruction was closer to expectations than the reconstruction achieved with the normalized Born approximation, for which the propagation model does not take optical heterogeneity into account. The second experiment was performed on a homogeneous phantom in a noncontact geometry. In this case, the reconstructed k^2 map showed an increase around the actual phantom boundary location, taking into account the boundary effects. The resulting fluorescence yield reconstruction was satisfactory in terms of shape and fluorophore position.

The method was also tested *in vivo* on small animal fDOT measurements performed on a nude mouse with a 14-day mammary murine lung tumor. In this experiment, the medium is highly heterogeneous and some uncertainties remain as to the identification of the detector elements in contact. The fluorescence yield reconstruction obtained with the optical heterogeneity correction conformed better to the mouse's lung and liver anatomy than the normalized Born method. The reconstructions performed with or without index matching liquid showed good consistency.

Future work will be focused on the integration of a laser scanner to measure the boundary of the studied medium thereby enabling fDOT measurements on mice without the compression plate, and the use of anatomical *a priori* information to improve the optical property map and/or constrain the fluorescence yield reconstruction.

This work was partly funded by CLARA, IPA project, Emil DiMI Network of Excellence and the RTB. The authors acknowledge J. L. Coll from INSERM U578 (Institute Albert Bonniot, Grenoble, France) and V. Josserand from ANIMAGE (Bron, France) for having provided, prepared, and carried out the mouse experiments. They also thank I. Texier-Nogues from CEA-LETI (Grenoble, France) for preparing the markers.

References

1. R. Weissleder and V. Ntziachristos, "Shedding light onto live molecular targets," Nat. Med. **9,** 123–128 (2003).
2. A. Godavarty, M. J. Eppstein, C. Zhang, A. B. Thomson, M. Gurfinkel, S. Theru, and E. M. Sevick-Muraca, "Fluorescence-enhanced optical imaging in large tissue volumes using a gain-modulated ICCD camera," Phys. Med. Biol. **48,** 1701–1720 (2003).
3. V. Ntziachristos, E. A. Schellenberger, J. Ripoll, D. Yessayan, E. Graves, A. Bogdanov, Jr., L. Josephson, and R. Weissleder, "Visualization of antitumor treatment by means of fluorescence molecular tomography with an annexin V-Cy5.5 conjugate," Proc. Natl. Acad. Sci. U.S.A. **101,** 12,294–12,299 (2004).
4. W. F. Cheong, S. A. Prahl, and A. J. Welch, "A review of the optical properties of biological tissues," IEEE J. Quantum Electron. **26,** 2166–2185 (1990).
5. S. R. Arridge, "Optical tomography in medical imaging," Inverse Probl. **15,** R41–R93 (1999).
6. S. R. Arridge and W. R. B. Lionheart, "Nonuniqueness in diffusion-based optical tomography," Opt. Lett. **23,** 882–884 (1998).
7. R. B. Schulz, J. Ripoll, and V. Ntziachristos, "Experimental fluorescence tomography of tissues with noncontact measurements," IEEE Trans. Med. Imaging **23,** 492–500 (2004).
8. R. Roy, A. Godavarty, and E. M. Sevick-Muraca, "Fluorescence-enhanced optical tomography using referenced measurements of heterogeneous media," IEEE Trans. Med. Imaging **22,** 824–836 (2003).
9. A. B. Milstein, S. Oh, K. J. Webb, C. A. Bouman, Q. Zhang, D. A. Boas, and R. P. Millane, "Fluorescence optical diffusion tomography," Appl. Opt. **42,** 3081–3094 (2003).
10. A. Godavarty, E. M. Sevick-Muraca, and M. J. Eppstein, "Three-dimensional fluorescence lifetime tomography," Med. Phys. **32,** 992–1000 (2005).
11. E. E. Graves, J. Ripoll, R. Weissleder, and V. Ntziachristos, "A submillimeter resolution fluorescence molecular imaging system for small animal imaging," Med. Phys. **30,** 901–911 (2003).
12. A. Soubret, J. Ripoll, and V. Ntziachristos, "Accuracy of fluorescent tomography in presence of heterogeneities: Study of the normalized Born ratio," IEEE Trans. Med. Imaging **24,** 1377–1384 (2005).
13. V. Ntziachristos and R. Weissleder, "Experimental three-dimensional fluorescence reconstruction of diffuse media by use of a normalized Born approximation," Opt. Lett. **26,** 893–895 (2001).
14. J. Ripoll, R. B. Schulz, and V. Ntziachristos, "Free-space propagation of diffuse light: theory and experiments," Phys. Rev. Lett. **91,** 103901.1–103901.4 (2003).
15. J. Ripoll and V. Ntziachristos, "From finite to infinite volumes: removal of boundaries in diffuse wave imaging," Phys. Rev. Lett. **96,** 173903 (2006).
16. R. C. Haskell, L. O. Svaasand, T. Tsay, T. Feng, M. S. McAdd-ams, and B. J. Tromberg, "Boundary conditions for the diffusion equation in radiative transfer," J. Opt. Soc. Am. A **11,** 2727–2741 (1994).
17. E. Scherleitner and B. G. Zagar, "Optical tomography imaging based on higher order Born approximation of diffuse photon density waves," IEEE Trans. Instrum. Meas. **54,** 1607–1611 (2005).
18. J. C. Ye, K. J. Webb, R. P. Millane, and T. J. Downar, "Modified distorted Born iterative method with an approximate Fréchet derivative for optical diffusion tomography," J. Opt. Soc. Am. A **16,** 1814–1826 (1999).
19. M. S. Patterson and B. W. Pogue, "Mathematical model for time-resolved and frequency-domain fluorescence spectroscopy in biological tissues," Appl. Opt. **33,** 1963–1974 (1994).
20. M. A. O'Leary, D. A. Boas, X. D. Li, B. Chance, and A. G. Yodh, "Fluorescence lifetime imaging in turbid media," Opt. Lett. **21,** 158–160 (1996).
21. M. A. O'Leary, *Imaging with Diffuse Photon Density Waves,* Ph.D. dissertation (University of Pennsylvania, 1996).
22. A. Da Silva, J. Boutet, A. Planat-Chrétien, J.-M. Dinten, and A. Glière, "Evaluation of a segmentation-based reconstruction scheme for fluorescence-enhanced diffuse optical tomography," Proc. SPIE **5859,** 246–255 (2005).
23. A. Koenig, L. Hervé, A. Da Silva, J.-M. Dinten, J. Boutet, M. Berger, J. L. Coll, V. Josserand, I. Texier-Nogues, P. Peltié, and P. Rizo, "Whole body animal examination by fluorescence tomography," presented at OSA Biomedical Optics Topical Meeting, Fort Lauderdale, Fla., USA, 19–23 March 2006.